

strength of magnetic fields for AXPs and that other properties determine whether a source is an AXP.

In spite of the current uncertainties, the optical identification offers us new insights into these enigmatic objects and motivates new observations and searches for optical pulsations. \square

Received 11 August; accepted 31 October 2000.

1. Mereghetti, S. in *Proc. NATO ASI School "The Neutron Star—Black Hole Connection"* (eds Kouveliotou, C., van Paradijs, J. & Ventura, J.) (Kluwer Academic Publishers, Dordrecht, 1999); also preprint astro-ph/9911252 at (xxx.lanl.gov) (1999).
2. Marsden, D., Lingenfelter, R. E., Rothschild, R. E. & Higdon, J. C. Nature vs. nurture: The origin of soft gamma-ray repeaters and anomalous X-ray pulsars. *Astrophys. J.* (submitted); also preprint astro-ph/9912207 at (xxx.lanl.gov) (1999).
3. Chatterjee, P., Hernquist, L. & Narayan, R. An accretion model for anomalous X-ray pulsars. *Astrophys. J.* **534**, 373–379 (2000).
4. Thompson, C. & Duncan, R. C. The soft gamma repeaters as very strongly magnetized neutron stars. II. Quiescent neutrino, X-ray, and alfvén wave emission. *Astrophys. J.* **473**, 322–342 (1996).
5. Wilson, C. A., Dieters, S., Finger, M. H., Scott, D. M. & van Paradijs, J. Rossi X-ray timing explorer observations of the anomalous pulsar 4U0142+61. *Astrophys. J.* **513**, 464–470 (1999).
6. Oke, J. B. et al. The Keck low-resolution imaging spectrometer. *Publ. Astron. Soc. Pacif.* **107**, 375–385 (1995).
7. Phelps, R. L. & Janes, K. A. Young open clusters as probes of the star formation process. I: An atlas of open cluster photometry. *Astrophys. J.* **90**, 31–82 (1994).
8. Fukugita, M., Shimasaku, K. & Ichikawa, T. Galaxy colors in various photometric band systems. *Publ. Astron. Soc. Pacif.* **107**, 945–958 (1995).
9. Cardelli, J. A., Clayton, G. C. & Mathis, J. S. The relationship between infrared, optical, and ultraviolet extinction. *Astrophys. J.* **345**, 245–256 (1989).
10. White, N. E., Angelini, L., Ebisawa, K., Tanaka, Y. & Ghosh, P. The spectrum of the 8.7 s X-ray pulsar 4U0142+61. *Astrophys. J.* **463**, L83–L86 (1996).
11. Predehl, P. & Schmitt, J. H. M. M. X-raying the interstellar medium: ROSAT observations of dust scattering halos. *Astron. Astrophys.* **293**, 889–905 (1995).
12. Perna, R., Hernquist, L. & Narayan, R. Emission spectra of fall back disks around young neutron stars. *Astrophys. J.* **541**, 344–350 (2000).
13. Vrtilek, S. D. et al. Observations of Cygnus X-2 with IUE—Ultraviolet results from a multiwavelength campaign. *Astron. Astrophys.* **235**, 162–173 (1990).
14. Hullerman, F., van Kerkwijk, M. H., Verbunt, F. W. M. & Kulkarni, S. R. A deep search for the optical counterpart to the anomalous X-ray pulsar 1E 2259+58.6. *Astron. Astrophys.* **358**, 605–611 (2000).
15. Mereghetti, S. & Stella, L. The very low mass X-ray binary pulsars: A new class of sources? *Astrophys. J.* **422**, L17–L20 (1995).
16. Stella, L., White, N. E. & Priedhorsky, W. The discovery of a 685 second orbital period from the X-ray source 4U 182030 in the globular cluster NGC 6624. *Astrophys. J.* **312**, L17–L21 (1987).
17. Paczynski, B. X-ray pulsar 1E 2259+58.6—A merged white dwarf with a 7 second rotation period? *Astrophys. J.* **365**, L9–L12 (1990).
18. Ferrario, L., Vennes, S., Wickramasinghe, D. T., Bailey, J. A. & Christian, D. J. EUVE J0317-855 A rapidly rotating, high-field magnetic white dwarf. *Mon. Not. R. Astron. Soc.* **292**, 205–217 (1997).
19. Pivovaroff, M. J., Kaspi, V. M. & Camilo, F. X-ray observations of the high magnetic field radio pulsar PSR J1814-1744. *Astrophys. J.* **535**, 379–384 (2000).
20. Bessell, M. S. in *Proc. IAU Coll. 136, Stellar Photometry—Current Techniques and Future Developments* (eds Butler, C. J. & Elliott, I.) 22–39 (Cambridge Univ. Press, Cambridge, 1992).
21. Schlegel, D. J., Finkbeiner, D. P. & Davies, M. Maps of dust infrared emission for use in estimation of reddening and cosmic microwave background radiation foregrounds. *Astrophys. J.* **500**, 525–553 (1998).
22. White, N. E. et al. A 25 min modulation from the vicinity of the unusually soft X-ray source X0142+614. *Mon. Not. R. Astron. Soc.* **226**, 645–654 (1987).
23. Motch, C. et al. A ROSAT glance at the galactic plane. *Astron. Astrophys.* **246**, L24–L27 (1991).
24. Van den Berg, M. & Verbunt, F. Spectroscopic confirmation of the optical identification of X-ray sources used to determine accurate positions for the anomalous X-ray pulsars 1E 2259+58.6 and 4U 0142+61. *Astron. Astrophys.* (submitted).
25. Monet, D. et al. USNO-A V2.0, *A Catalog of Astrometric Standards* (US Naval Observatory Flagstaff Station (USNOFS) and Universities Space Research Association (USRA) stationed at USNOFS, 2000).
26. Baraffe, I., Chabrier, G., Allard, F. & Hauschildt, P. H. Evolutionary models for solar metallicity low-mass stars: mass-magnitude relationships and color-magnitude diagrams. *Astron. Astrophys.* **337**, 403–412 (1998).
27. Bergeron, P., Wesemael, F. & Beauchamp, A. Photometric calibration of hydrogen- and helium-rich white dwarf models. *Publ. Astron. Soc. Pacif.* **107**, 1047–1054 (1995).
28. Stetson, P. B. DAOPHOT—A computer program for crowded-field stellar photometry. *Publ. Astron. Soc. Pacif.* **99**, 191–222 (1987).
29. Stetson, P. B. Homogeneous photometry for star clusters and resolved galaxies. II. Photometric standard stars. *Publ. Astron. Soc. Pacif.* **112**, 925–931 (2000).

Acknowledgements

We thank D. Kaplan for undertaking the observations at the 60-inch telescope, and acknowledge helpful discussions with B. Paul and F. Verbunt. Model atmospheres for hot white dwarfs were kindly provided by J. Heise. The observations were obtained at the W.M. Keck Observatory on Mauna Kea, Hawaii, which is operated by the California Association for Research in Astronomy. This research made use of the SIMBAD data base. M.H.V.K. is supported by the Royal Netherlands Academy of Science (KNAW). S.R.K.'s research is supported, in part, by grants from the National Science Foundation and the National Aeronautics and Space Administration.

Correspondence and requests for materials should be addressed to F.H. (e-mail: f.hullerman@astro.uu.nl).

Direct observation of growth and collapse of a Bose–Einstein condensate with attractive interactions

Jordan M. Gerton*, Dmitry Strekalov*†, Ionut Prodan* & Randall G. Hulet*

* Physics and Astronomy Department and Rice Quantum Institute, MS 61, Rice University, Houston, Texas 77251, USA
† Present address: Jet Propulsion Laboratory, MS 300-123, Pasadena, California 91109, USA.

Quantum theory predicts that Bose–Einstein condensation of a spatially homogeneous gas with attractive interactions is precluded by a conventional phase transition into either a liquid or solid¹. When confined to a trap, however, such a condensate can form², provided that its occupation number does not exceed a limiting value^{3,4}. The stability limit is determined by a balance between the self-attractive forces and a repulsion that arises from position–momentum uncertainty under conditions of spatial confinement. Near the stability limit, self-attraction can overwhelm the repulsion, causing the condensate to collapse^{5–8}. Growth of the condensate is therefore punctuated by intermittent collapses^{9,10} that are triggered by either macroscopic quantum tunnelling or thermal fluctuation. Previous observations of growth and collapse dynamics have been hampered by the stochastic nature of these mechanisms. Here we report direct observations of the growth and subsequent collapse of a ^7Li condensate with attractive interactions, using phase-contrast imaging. The success of the measurement lies in our ability to reduce the stochasticity in the dynamics by controlling the initial number of condensate atoms using a two-photon transition to a diatomic molecular state.

Condensate growth is initiated by cooling the gas below the critical temperature T_c for Bose–Einstein condensation (BEC). For

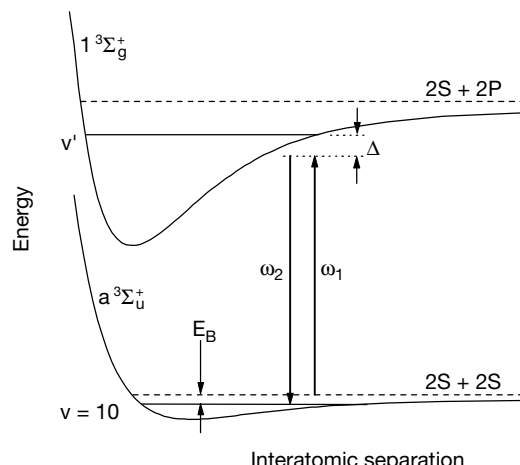


Figure 1 Two-photon molecular association technique. Two atoms in the electronic ground state ($2S + 2S$) interact along the $a^3\Sigma_u^+$ diatomic molecular potential at the dissociation limit indicated by the dashed line. They may be associated into the least-bound vibrational level, $v = 10$, when the relative frequency between two drive lasers, $\omega_1 - \omega_2$, is equal to E_B , where $E_B \approx 12.47$ GHz is the binding energy of the $v = 10$ level. Each laser is tuned near resonance with a vibrational level $v' = 72$ of the $1^3\Sigma_g^+$ excited state potential, which correlates to $2S + 2P$ atomic states. The intensity of each laser beam is between 0.5 and 2.5 W cm^{-2} and the intermediate state detuning $\Delta \approx -110$ MHz.

attractive interactions, the number of condensate atoms N_0 grows until the condensate collapses. During the collapse, the density rises, giving a sharp increase in the rate of collisions, both elastic and inelastic. These collisions cause atoms to be ejected from the condensate in an energetic explosion. The physics that determines both the stability condition and the dynamical process of collapse of the condensate bears some similarity to that of a star going supernova¹¹, even though the time, length, and energy scales for these two phenomena are very different. In the stellar case, the stability criterion is provided by a balance between the pressure due to the quantum degeneracy of electrons that make up the star and gravitational attraction. If the mass of the star exceeds the stability limit¹², the star collapses, releasing nuclear energy and triggering a violent explosion. In contrast to the stellar case, the condensate regrows after a collapse as it is fed by collisions between thermal atoms in the gas, and a series of sawtooth-like cycles of growth and collapse will continue until the gas reaches thermal equilibrium^{9,10}. We previously attained evidence for this nonequilibrium dynamical behaviour in ^7Li by measuring the distribution of N_0 at selected times after a fast quench of the gas¹³. N_0 was found to be distributed between small numbers, $N_0 \approx 100$, and the maximum number of $\sim 1,250$ atoms, in agreement with the growth and collapse model.

The process of making reliable measurements of such small values of N_0 destroys the condensate, preventing an observation of condensate dynamics in real time. Although the phase-contrast imaging technique employed here has been used for (nearly) nondestructive measurements of large condensates¹⁴, a few incoherent photons are always scattered, and these heat the gas. As the phase-contrast signal is proportional to the number of scattered photons, achieving sufficient sensitivity to small condensates, such as those studied here, results in excessive heating and destruction of the condensate¹⁵. Here, direct observation of the dynamics is made possible by dumping the condensate, while only slightly affecting the thermal atoms. This synchronizes the growth and collapse cycles for different experiments at a particular point in time. The subsequent growth/collapse dynamics are then obtained by repeating the experiment and measuring N_0 at different delays following the dump pulse. In a recent experiment with essentially pure condensates of ^{85}Rb atoms, a magnetically tuned Feshbach resonance was used to suddenly switch the interactions from repulsive to attractive, thereby inducing a collapse at a specified time¹⁶. In that experiment, condensates are produced with N_0 far greater than the stability limit, and consequently with high initial energy. In

contrast, for the present experiment, the collapse occurs with N_0 below the maximum number by macroscopic quantum tunnelling or thermal fluctuation^{7–9}. Furthermore, the condensate coexists with a gas of thermal atoms, allowing the kinetics to be probed.

The apparatus used to produce BEC of ^7Li has been described previously¹⁵. Permanent magnets establish an Ioffe-Pritchard type trap with a nearly spherically symmetric, harmonic trapping potential. Approximately 2.5×10^8 atoms in the $F = 2$, $m_F = 2$ hyperfine sublevel of ^7Li are directly loaded into the trap from a laser-slowed atomic beam. Following loading, the atoms are evaporatively cooled to ~ 400 nK with $\sim 4 \times 10^5$ atoms using a microwave field to selectively spin-flip and remove the most energetic atoms. Under these conditions, the gas is quantum degenerate. The microwave frequency is maintained at the end frequency for two seconds after evaporation, and is subsequently lowered during a quench pulse 100 ms in duration that removes all but the coldest $\sim 10^5$ atoms. This leaves the gas far from thermal equilibrium, and if left to freely evolve, the condensate will alternately grow and collapse many times over a period of ~ 30 s (ref. 13).

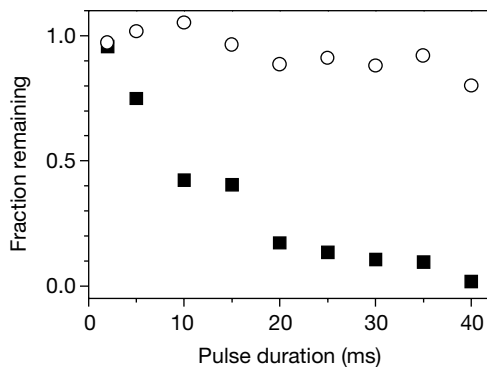


Figure 2 Energy selectivity of the two-photon light pulse. The fraction of condensate atoms (solid squares) and total atoms (open circles) which remain trapped immediately after a light pulse is plotted as a function of the light pulse duration. Each data point is an average of five separate experiments normalized to measurements taken without the light pulse. For these measurements, $N = (7 \pm 1) \times 10^4$ atoms. Achieving the necessary energy selectivity required the two diode lasers used to drive the two-photon transition to be phase-locked. When locked, the relative frequency spectrum of the two lasers was measured to be less than 1 Hz in width.

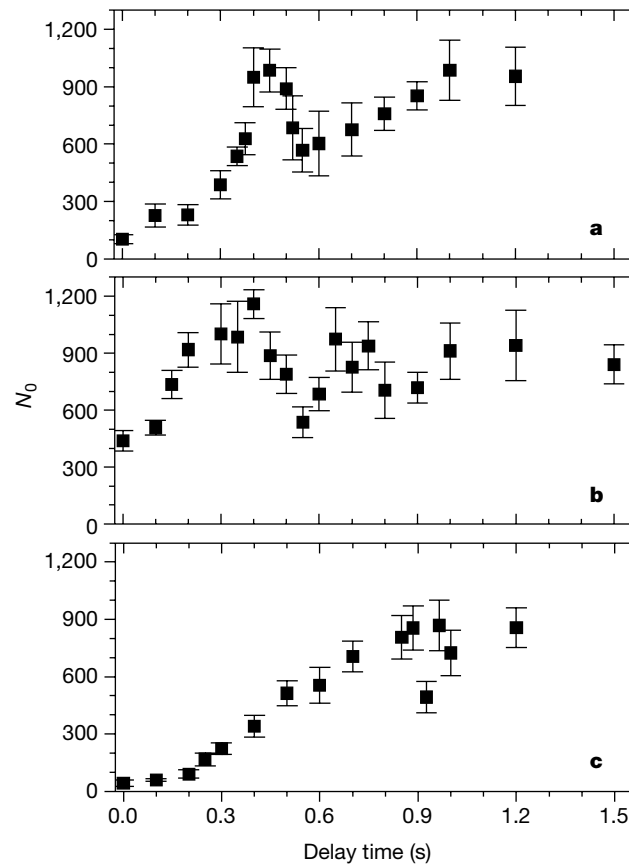


Figure 3 Condensate growth and collapse dynamics. Each data point is the mean of five measurements for the same delay time following the light pulse, and the error bars are the standard deviation of the mean. **a**, N_0 is reduced to ~ 100 atoms using the two-photon light pulse. The reduction in N_0 after the first peak at 450 ms is a direct manifestation of collapse. **b**, The condensate is only partially dumped in order to speed up the initial growth. Subsequent maxima and minima are observed as the gas continues to undergo growth and collapse cycles while evolving towards thermal equilibrium. **c**, The light pulse duration is increased, so that the condensate is dumped completely, to within the experimental resolution. We note the slow turn-on of growth and the subsequent saturation in the growth rate (see text). For **a** and **c**, there is a 3-s delay following the microwave quench pulse before the light pulse; whereas in **b**, the delay is 5 s. Additionally, for **a** and **c**, $N = (7 \pm 1) \times 10^4$ atoms and $T = (170 \pm 15)$ nK immediately before the light pulse, while for **b**, $N = (1.0 \pm 0.1) \times 10^5$ atoms and $T = (200 \pm 20)$ nK. For each individual image, the statistical uncertainty in N_0 is ± 60 atoms, while the systematic uncertainty, dominated by uncertainties in the imaging system, is $\pm 20\%$ ¹³.

Destructive phase-contrast imaging is used to determine N_0 , the total number of atoms N , and their temperature T (ref. 15).

Following a delay of several seconds after the microwave quench pulse, the condensate is dumped by a light pulse consisting of two co-propagating laser beams whose frequency difference is tuned to resonance between the collisional state of two free atoms and a vibrational level of the diatomic molecule Li₂, as shown in Fig. 1. Once in the molecular state, the laser of frequency ω_2 can stimulate a single-photon transition to the intermediate level v' , which may spontaneously decay, most probably into a state of two energetic atoms that will escape the trap. This method for removing atoms is very energy-specific because the observed two-photon linewidth of ≤ 500 Hz is much less than the ~ 5 kHz thermal energy spread of the trapped atoms. In particular, the condensate may be selectively removed without significantly affecting the remaining atoms. This is demonstrated in Fig. 2, where both the measured condensate fraction and the fraction of total atoms are plotted as a function of the duration of the light pulse. The two-photon spectroscopy of this work is similar to that performed previously in a non-quantum-degenerate gas of lithium atoms at $T \approx 1$ mK (ref. 17), and in a Bose condensate of Rb atoms¹⁸.

After the light pulse, the gas is allowed to evolve freely for a certain time, at which point a destructive measurement of N_0 is made. Figure 3a shows the dynamical evolution of the condensate after a

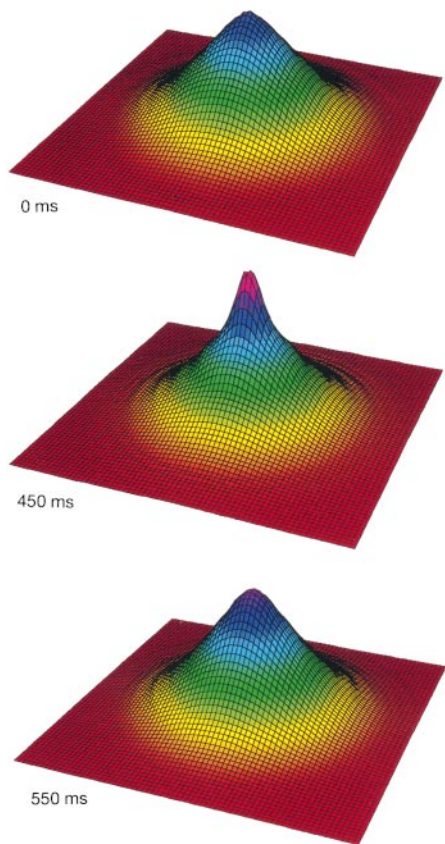


Figure 4 Phase-contrast images. These images were selected from those used to construct Fig. 3a. The upper image corresponds to data immediately after the dump pulse (0 ms), the middle image to the peak of condensate growth (450 ms), and the lower image to the first collapse (550 ms). The fitted values of N_0 are 40, 1,210 and 230 atoms for the upper, middle and lower images, respectively. The displayed images result from angle-averaging the actual images about the probe laser propagation axis and the signal height is proportional to the column density of the atom cloud integrated along this direction⁴. The image area corresponds to a square of sides 85 μm . A movie of the growth and collapse was produced using representative time-ordered images from the data of Fig. 3a, and is available for viewing at <http://atomcool.rice.edu/collapse.html>.

light pulse whose duration is adjusted to reduce N_0 to an initial value of ~ 100 atoms. N_0 increases immediately after the light pulse as the condensate is fed by collisions between noncondensed thermal atoms, reaching a maximum value consistent with the expected upper limit of 1,250 atoms. A collapse is clearly indicated by the subsequent reduction in N_0 . After the collapse, N_0 grows again, as the gas is not yet in thermal equilibrium. Figure 4 shows representative phase-contrast images taken from the data in Fig. 3a for the specified delay times. The central peak, most clearly visible at 450 ms delay, corresponds to the condensate.

The condensate growth rate may be adjusted by varying the duration of the light pulse. By reducing the duration, fewer atoms are removed from both the condensate and from the low-energy thermal atoms that directly contribute to condensate growth, and consequently the growth rate increases. This is shown in Fig. 3b, where two secondary peaks are now discernible. For Fig. 3c, the light pulse duration is lengthened, causing more atoms to be removed, and slowing the rate of growth.

Each data point in Fig. 3 is the mean of five separate measurements of N_0 . Consequently, these data represent an average of many trajectories whose initial phase and rate of growth differ slightly. To analyse the results, we numerically simulate the collisional redistribution of atoms over the energy states of the trap using the quantum Boltzmann equation, as described in detail elsewhere⁹. The coloured curves shown in Fig. 5 are a sample of simulated trajectories which include the effect of the microwave quench pulse and the light pulse. The variation in condensate growth following a light pulse is mainly the result of slight differences in initial conditions that lead to variations in the energy distribution of atoms in the trap. Additionally, the stochastic nature of the collapse process, which causes each collapse to occur at a slightly different value of N_0 , contributes to dephasing of different trajectories. The heavy black line represents the average of 40 trajectories obtained by running the simulation several times with slightly different initial conditions. In the simulations, N_0 is set to 100 atoms immediately following the light pulse in order to provide direct comparison with the data in Fig. 3a. Additionally, N_0 is set to 200 atoms immediately after a collapse in order to achieve the best agreement with our previous statistical studies¹³. The only adjustable parameter in the simulations was the fraction of thermal atoms lost within the spectral width of the two-photon transition.

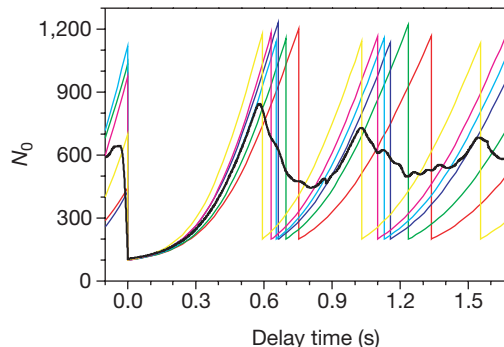


Figure 5 Simulation of condensate dynamics. The coloured curves show individual trajectories generated by a numerical quantum Boltzmann simulation, which models the kinetics of evaporative cooling and thermal equilibration. Individual trajectories were generated by running the simulation for 40 different initial values of N spaced evenly between 2.4×10^8 and 2.6×10^8 atoms. The resulting values of N just before the light pulse range between 6×10^4 and 8×10^4 atoms, in agreement with the range of N observed in the data. The heavy solid line is the mean of these 40 trajectories. The effect of the light pulse on the thermal atoms is simulated by instantaneously reducing the population of atoms within a 500 Hz wide Lorentzian energy band, consistent with the observed spectral width. For the simulation shown, 90% of the thermal atoms at the Lorentzian peak are lost.

The simulation results agree well with the data in several respects. The data in Fig. 3b show that each subsequent peak following the initial growth is slightly lower, as the trajectories corresponding to each individual measurement dephase from one another. This dephasing causes the maxima (minima) to occur at smaller (larger) values of N_0 than for any individual trajectory. This behaviour is seen in the simulation average shown in Fig. 5, confirming our understanding of the role of averaging in these measurements.

Condensate growth should be affected by the quantum statistical effect known as Bose enhancement: the condensate growth rate scales with the occupation number N_0 . This would lead to an exponentially increasing growth rate, which is, however, neither observed in the data nor predicted by the quantum Boltzmann equation model. For the conditions shown in Fig. 3c, for example, both the model and the data show a saturation in the growth rate when N_0 becomes larger than ~ 150 atoms. An analysis of the distribution of atoms among the trap energy levels in the model simulations indicates that the condensate is fed mostly by collisions between atoms with the lowest energies. Further, this analysis indicates that when the low-energy population is depleted, the growth is limited by the rate for non-Bose-enhanced 'trickle-down' collisions between high-energy atoms. Owing to our high sensitivity to small values of N_0 , the very early stages of condensate growth following the dump can be observed, illuminating this subtle, yet important, departure from the pure Bose enhancement prediction. The first observation of condensate growth¹⁹ could not detect small values of N_0 and therefore was not sensitive to the initial stages of growth.

To our knowledge, the data presented here are the first direct observations of the growth and collapse of Bose-Einstein condensates with attractive interactions. By enabling the preparation of condensates with a desired mean number of atoms with minimal perturbation to the noncondensed atoms, the two-photon technique provides a new way of studying the dynamics of this non-equilibrium and stochastic quantum system. □

Received 12 September; accepted 24 October 2000.

1. Stoof, H. T. C. Atomic Bose gas with a negative scattering length. *Phys. Rev. A* **49**, 3824–3830 (1994).
2. Bradley, C. C., Sackett, C. A., Tollett, J. J. & Hulet, R. G. Evidence of Bose-Einstein condensation in an atomic gas with attractive interactions. *Phys. Rev. Lett.* **75**, 1687–1690 (1995).
3. Ruprecht, P. A., Holland, M. J., Burnett, K. & Edwards, M. Time-dependent solution of the nonlinear Schrödinger equation for Bose-condensed trapped neutral atoms. *Phys. Rev. A* **51**, 4704–4711 (1995).
4. Bradley, C. C., Sackett, C. A. & Hulet, R. G. Bose-Einstein condensation of lithium: observation of limited condensate number. *Phys. Rev. Lett.* **78**, 985–989 (1997).
5. Kagan, Y., Shlyapnikov, G. V. & Walraven, J. T. M. Bose-Einstein condensation in trapped atomic gases. *Phys. Rev. Lett.* **76**, 2670–2673 (1996).
6. Shuryak, E. V. Bose condensate made of atoms with attractive interaction is metastable. *Phys. Rev. A* **54**, 3151–3154 (1996).
7. Stoof, H. T. C. Macroscopic quantum tunneling of a Bose condensate. *J. Stat. Phys.* **87**, 1353–1366 (1997).
8. Ueda, M. & Leggett, A. J. Macroscopic quantum tunneling of a Bose-Einstein condensate with attractive interactions. *Phys. Rev. Lett.* **80**, 1576–1579 (1998).
9. Sackett, C. A., Stoof, H. T. C. & Hulet, R. G. Growth and collapse of a Bose condensate with attractive interactions. *Phys. Rev. Lett.* **80**, 2031–2034 (1998).
10. Kagan, Y., Muryshev, A. E. & Shlyapnikov, G. V. Collapse and Bose-Einstein condensation in a trapped Bose gas with negative scattering length. *Phys. Rev. Lett.* **81**, 933–937 (1998).
11. Houbiers, M. & Stoof, H. T. C. Stability of Bose condensed atomic ⁷Li. *Phys. Rev. A* **54**, 5055 (1996).
12. Chandrasekhar, S. *An Introduction to the Study of Stellar Structure* (Dover, New York, 1957).
13. Sackett, C. A., Gerton, J. M., Welling, M. & Hulet, R. G. Measurements of collective collapse in a Bose-Einstein condensate with attractive interactions. *Phys. Rev. Lett.* **82**, 876–879 (1999).
14. Andrews, M. R. et al. Direct, nondestructive observation of a Bose condensate. *Science* **273**, 84–87 (1996).
15. Sackett, C. A., Bradley, C. C., Welling, M. & Hulet, R. G. Bose-Einstein condensation of lithium. *Appl. Phys. B* **65**, 433–440 (1997).
16. Cornish, S. L., Claussen, N. R., Roberts, J. L., Cornell, E. A. & Wieman, C. E. Stable ⁸⁵Rb Bose-Einstein condensates with widely tunable interactions. *Phys. Rev. Lett.* **85**, 1795–1798 (2000).
17. Abraham, E. R. I., McAlexander, W. I., Sackett, C. A. & Hulet, R. G. Spectroscopic determination of the s-wave scattering length of lithium. *Phys. Rev. Lett.* **74**, 1315–1318 (1995).
18. Wynar, R., Freeland, R. S., Han, D. J., Ryu, C. & Heinzen, D. J. Molecules in a Bose-Einstein condensate. *Science* **287**, 1016–1019 (2000).
19. Miesner, H.-J. et al. Bosonic stimulation in the formation of a Bose-Einstein condensate. *Science* **279**, 1005–1007 (1998).

Acknowledgements

We thank C.A. Sackett for help with the quantum Boltzmann simulation. This work was supported by the US National Science Foundation, the National Aeronautics and Space Administration, the Office of Naval Research and the Welch Foundation.

Correspondence and requests for materials should be addressed to R.G.H. (e-mail: randy@atomcool.rice.edu).

Direct observation of molecular cooperativity near the glass transition

E. Vidal Russell & N. E. Israeloff

Department of Physics and Center for Interdisciplinary Research on Complex Systems, Northeastern University, Boston, Massachusetts 02115, USA

The increasingly sluggish response of a supercooled liquid as it nears its glass transition¹ (for example, refrigerated honey) is prototypical of glassy dynamics found in proteins, neural networks and superconductors. The notion that molecules rearrange cooperatively has long been postulated² to explain diverging relaxation times and broadened (non-exponential) response functions near the glass transition. Recently, cooperativity was observed and analysed in colloid glasses³ and in simulations of binary liquids well above the glass transition⁴. But nanometre-scale studies of cooperativity at the molecular glass transition are lacking⁵. Important issues to be resolved include the precise form of the cooperativity and its length scale⁶, and whether the broadened response is intrinsic to individual cooperative regions, or arises only from heterogeneity^{7–9} in an ensemble of such regions. Here we describe direct observations of molecular cooperativity near the glass

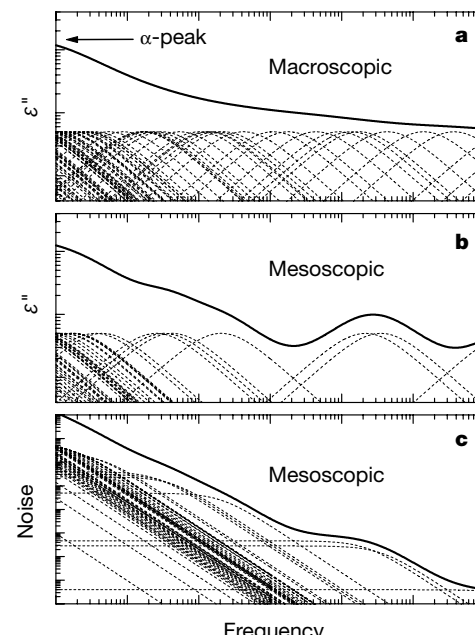


Figure 1 Heterogeneous scenario. **a**, The imaginary component of the dielectric susceptibility, ϵ'' , is assumed to arise from a superposition of Debye peaks. In a mesoscopic sample (**b**), the individual Debye peaks become apparent as spectral features, particularly in the high-frequency tail of the α -peak. In the thermal noise spectrum (**c**) the Debye peaks appear as Lorentzians, which also produce spectral features.